ACS APPLIED MATERIALS & INTERFACES

Research Article

Cite This: ACS Appl. Mater. Interfaces 2018, 10, 13361−13372

www.acsami.org

Porous Nanogold/Polyurethane Scaffolds with Improved Antibiofilm, Mechanical, and Thermal Properties and with Reduced Effects on Cell Viability: A Suitable Material for Soft Tissue Applications

L. Tamayo,[*,†,⊥] D. Acuña,[‡] A. L. Riveros,[§] M. J. Kogan,[§] M. I. Azócar,[∥] M. Páez,[∥] M. Leal,[⊥] M. Urzúa,[*,⊥] and E. Cerda[‡]

[†]Facultad de Ingeniería, Instituto de Ciencias Químicas Aplicadas, Polymers and Macromolecules Center, Universidad Autónoma de Chile, El Llano Subercaseaux 2801, San Miguel, Santiago 8910060, Chile

[‡]Departamento de Física, Universidad de Santiago, Av. Ecuador 3493, Santiago 8320000, Chile

[§]Facultad de Ciencias Químicas y Farmacéuticas, Advanced Center for Chronic Diseases (ACCDiS), Universidad de Chile, Santos Dumont 964, Casilla 233, Santiago 8320000, Chile

[∥]Departamento de Química de los Materiales, Facultad de Química y Biología, Universidad de Santiago de Chile, Av. L. B. O'Higgins 3363, Casilla 40, Correo 33, Santiago 8320000, Chile

[⊥]Departamento de Química, Facultad de Ciencias, Universidad de Chile, Las Palmeras 3425, Casilla 653, Santiago 8320000, Chile

Supporting Information

ABSTRACT: The use of implants carries on a series of problems, among them infections, poor biocompatibility, high levels of cytotoxicity, and significant mechanical differences between implants and host organs that promote stress shielding effects. These problems indicate that the materials used to make implants must meet essential requirements and high standards for implantations to be successful. In this work, we present the synthesis, characterization and evaluation of the antibiofilm, mechanical, and thermal properties, and cytotoxic effect of a nanocomposite-based scaffold on polyurethane (PU) and gold nanoparticles (AuNPs) for soft tissue applications. The effect of the quantity of AuNPs on the antibacterial activity of nanocomposite scaffolds was evaluated against *Staphylococcus epidermidis* and *Klebsiella* spp., with a resulting 99.99% inhibition of both bacteria using a small quantity of nanoparticles. Cytotoxicity was evaluated with the T10 1/2 test against fibroblast cells. The results demonstrated that porous nanogold/PU scaffolds have no toxic effects on fibroblast cells to the 5 day exposition. With respect to mechanical properties, stress−strain curves showed that the compressive modulus and yield strength of PU scaffolds were significantly enhanced by AuNPs (by at least 10 times). This is due to changes in the arrangement of hard segments of PU, which increase the stiffness of the polymer. Thermogravimetric analysis showed that the degradation onset temperature rises with an increase in the quantity of AuNPs. These properties and characteristics demonstrate that porous nanogold/PU scaffolds are suitable material for use in soft tissue implants.

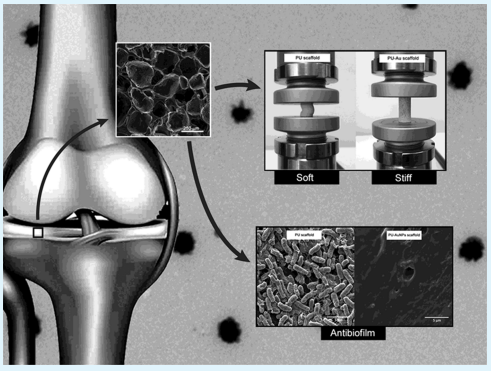

KEYWORDS: *biomaterials, porous scaffolds, gold nanoparticles, antibiofilm, non-cytotoxic, mechanical properties*

1. INTRODUCTION

Biomaterials in the form of implants are widely used to replace and/or restore the function of traumatized and damaged tissue and organs and thus improve the quality of life of patients. Biomaterials used in implants like menisci, vascular grafts, and bones must prevent the proliferation of bacteria and subsequent infections. They should not be toxic to the surrounding tissue and ideally, and they should promote the adhesion of host tissue. In addition, they must be able to withstand the mechanical stress of the body.

Considering that biomaterials are designed to be used in intimate contact with tissue, it is essential that the implanted material does not have any harmful effects on host tissue and organs. Thus, one of the essential attributes of biomaterials used in tissue engineering is the capability to encourage cells to adhere to the biomaterial surface.[1] The inability of cells to adhere to a matrix induces apoptosis.[2,3]

The biocompatible characteristic of biomaterials associated with the spontaneous formation of a protein layer under physiological conditions can promote the colonization of microorganisms and biofilm formation, where the latter protects bacteria from antimicrobial agents.[4] Considering the

Received: February 7, 2018
Accepted: April 7, 2018
Published: April 7, 2018

DOI: 10.1021/acsami.8b02347
ACS Appl. Mater. Interfaces 2018, 10, 13361−13372

susceptibility of some biomaterials to bacterial colonization and the consequent occurrence of infections, it is ideal that the biomaterials have the capacity to inhibit adhesion of pathogens to their surface and prevent biofilm formation. Biofilm is the main cause of healthcare-associated infections (HAIs) and implant failure. In 2008, the European Centre for Disease Prevention and Control reported that an estimated 4.1 million patients acquire HAIs annually in European hospitals, with an estimated 370 000 deaths annually as a direct result.[5] This demonstrates the need to develop implant biomaterials that can prevent or inhibit the proliferation of microorganisms to avoid infection and implant failure.

Another important issue about biomaterials is their mechanical properties, because they must endure the mechanical conditions of the body. For example, bones are subjected to stresses of approximately 4 MPa. The mean load on a hip joint is up to 3 times one's body weight (3000 N), and the peak load with jumping can be as high as 10 times one's body weight.[6]

Menisci play an important role in weight-bearing and stability in the knee.[7] For example, a knee joint deficient in cruciate ligament and menisci is associated with more rapid cartilage loss, leading to the development of knee arthrosis. Human menisci present a compression module of 0.22 MPa[8] and typically experience loads 2−5 times that of body weight, which translates into approximately 1200−3000 N of force.[9] In general, the control over stiffness of materials in this kind of implant is an important requirement. Nevertheless, differences in stiffness between the implant and the adjacent organ result in the implant loosening, leading to revision surgery.[10] Therefore, the mismatch between implant biomaterials and tissue must be minimal.

Polymers such as poly(lactic acid) (PLA), poly(lactic-*co*-glycolic acid) (PLGA), and polycaprolactone (PCL) have been used for the fabrication of biomaterials exhibiting some of these properties.[11−13] For example, porous PLGA scaffolds have been used for proliferation of Nucleus Pulposus cells with adequate mechanical properties for herniated lumbar disc. PLA has been used for the manufacture of scaffolds with positive effects on the adhesion and proliferation of fibroblast cells.[11] Polyurethanes (PUs) are among the most popular materials for biomedical applications because of their excellent biocompatible and mechanical properties.[14] PUs used in implants of menisci, bones, and ligaments must have porous structures that promote cellular regeneration. However, porous scaffold materials reduce mechanical properties because of the inherent brittleness of materials with low levels of compaction. Hence, the mechanical properties of the scaffold must be enhanced to match the material properties of the replaced tissue. Because the stiffness of synthetic polymers decreases with increasing porosity,[15,16] a strategy to improve their mechanical properties is incorporating inorganic fillers like calcium phosphate, hydroxyapatite, and Bioglass.[17,18] Nanostructures like nanosilica,[19] hydroxyapatite,[20] spherical TiO_2, carbon nanofibers, and nanoclay[21] have been incorporated into PU matrices to improve the mechanical properties of the polymer. The improvement of mechanical properties with these materials is related to the greater stiffness of the nanoparticles and the increased area of matrix−nanostructure interface and the strong interaction between them. Several models have been employed to explain the mechanical properties of nanocomposites that consider factors like the aspect ratio of nanofillers, mixture law, dispersion, and others.[22]

The incorporation of metallic nanofillers like silver, copper, and gold nanoparticles (AuNPs) in polymeric matrices has been shown to provide the polymer with responsiveness against bacterial adhesion and proliferation. Composites of cellulose and silver nanoparticles have been used to make scaffolds of tissue with antibacterial activity against *Escherichia coli*.[23] Other materials based on polyacrylates and silver nanoparticles have shown antibacterial and healing properties in wounds of rats.[24] Silver−copper hybrid core−shell nanoparticles have also been incorporated into polydopamine to make materials with antibacterial and antibiofilm capacity; the rapid release of copper ions and the more controlled release of silver ions have shown excellent results against *E. coli* and *S. aureus*.[25] The antibacterial effects of metallic nanofillers include rupturing bacterial walls and membranes, generating reactive oxygen species, forming condensed DNA, and inhibiting ATP synthesis, among others.[26−28] AuNPs are of particular interest because of their antibacterial capability and the absence of any toxic effect on epithelial and fibroblast cells.[29,30] In addition, the surfaces of AuNPs can be modified in function of compatibility with the matrix.

Considering that the biomaterials used in medical implants to restore or replace menisci, bones, or ligaments are susceptible to bacterial proliferation and the consequent possibility of infection[31] and bearing in mind that porous morphology of biomaterials reduces their stiffness, we studied the effect of adding AuNPs with sea urchin-shaped morphology to the porous matrices of PU, with the aim of evaluating the antibacterial, mechanical, thermal, hydrophobic/hydrophilic, and cytotoxic properties of the nanocomposite. Antibacterial assays were performed against *Staphylococcus epidermidis* and *Klebsiella* spp., both pathogen bacteria associated with implant infections. Because most cartilage around menisci is surrounded by fibrous perichondrium, a tissue layer composed of fibroblasts and collagen, we chose T10 1/2 fibroblast cells for cytotoxicity assays. Mechanical properties were evaluated by compression tests according to ASTM standard D695-10.

2. EXPERIMENTAL SECTION

2.1. Materials. The following materials were purchased from Sigma-Aldrich: PCL diol with M_n of ca. 530, 1,4-butanediol and 1,6-hexamethylene diisocyanate (HMDI) with M_w of 168.9 g/mol, dimethyl sulfoxide (DMSO) ReagentPlus (≥99.5%), silver nitrate, sodium citrate, adenine, L-ascorbic acid, potassium carbonate, hydrogen tetrachloroaurate(III) trihydrate ($HAuCl_4$), sodium tetrahydroborate, and gelatin.

2.2. Synthesis of AuNPs. AuNPs were synthetized by chemical reduction of $HAuCl_4$ by L-ascorbic acid in a two-step process. First, 25 mg of K_2CO_3 was dissolved in 10 mL of deionized water. Then, 1.5 mL of an aqueous solution 0.02 M was added. The solution was stored under darkness for 24 h. Finally, this solution was added into 50 mL of DMSO followed by addition of 2 mL of silver seed, 8 mL of gelatin type B solution at 2 w/v %, and 2 mL of ascorbic acid 0.1 M, without stirring. The silver seeds were prepared according to the methodology outlined by Lu.[32]

2.3. Synthesis and Characterization of PU. PU was prepared by the two-step polymerization method. First, 6.9 g of PCL was mixed with 15 g of HMDI at 80 °C for 4 h under a nitrogen atmosphere to form a prepolymer. Then, 1,4-butanediol (0.6 g) was added to the prepolymer with rapid stirring at 80 °C for 72 h to obtain a PU polymer. The molecular weight and polydispersity index (PDI) were measured using gel permeation chromatography (Agilent, model 1100, USA) using dimethylformamide with 0.1 M LiBr as an eluent at a flow rate of 1.0 mL/min at 40 °C, and monodispersive polystyrene as the

DOI: 10.1021/acsami.8b02347
ACS Appl. Mater. Interfaces 2018, 10, 13361−13372

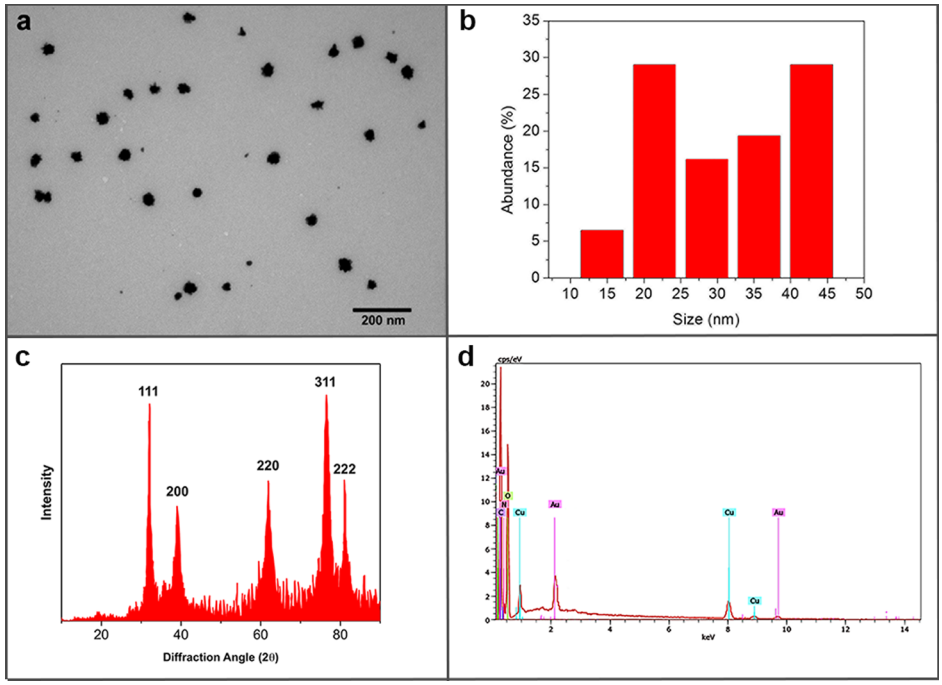

Figure 1. (a) SEM image of sea urchin-shaped AuNPs stabilized by gelatin, (b) size distribution histogram, (c) XRD pattern of AuNPs, and (d) EDS spectrum of AuNPs.

calibration standards. The number average molecular weight of PU was 156 kg/mol with a PDI of 2.2.

2.4. Preparation of Porous Nanogold/PU Scaffolds. Different quantities of AuNPs (0.16−0.64 wt %) were mixed with 2 g of PU in DMSO at 70 °C in. The mixture was incorporated into a cylindrical Teflon template and cooled at −18 °C. Porous samples were obtained by incorporating 11 g of sodium chloride (sieved to 50−300 μm) in a gold−PU mixture. The cylindrical porous samples were washed several times in an ethanol/water solution (30/70%) until complete dissolution of NaCl crystals. PU and nanocomposites containing 0.16, 0.32, and 0.64 wt % of AuNPs were labeled PU, PU−Au 0.16, PU−Au 0.32, and PU−Au 0.64, respectively.

2.5. Porosity. The porosity of scaffolds was measured by the liquid displacement method, according to the method described by Salehi.[33] It consists in immersing the samples in ethanol, which easily penetrates the pores of the sample without dissolving the polymer. The porosity is represented by eq 1; here, V_1 corresponds to the initial volume of ethanol, V_2 is the cylinder volume, and V_3 is the final residual volume after removing the impregnated ethanol cylinder.

$$\varepsilon = (V_1 - V_3)/(V_2 - V_3) \times 100 \quad (1)$$

2.6. Characterization of Morphology. AuNPs were characterized by transmission electron microscopy (TEM; Philips Tecnai 12). Porous nanocomposites were coated with a thin film of Pt/Pd and characterized by scanning electron microscopy (SEM; VEGA3 TESCAN). The compositional distributions of AuNPs and their dispersion into PU were analyzed by energy-dispersive X-ray spectroscopy (EDS) in a JEOL JSM-IT300LV with an EDS Aztec Oxford detector.

2.7. Thermal Characterization. A differential scanning calorimeter (TA Instruments, model Q20) was used to evaluate the thermal characteristics of the samples. The measurements were made with a constant nitrogen flow with a heating rate of 10 °C/min from −50 to 350 °C. The thermal degradation of samples was analyzed by thermogravimetric analysis (TGA; TA Instruments, model Q50). Samples weighing 8−10 mg were heated at a rate of 10 °C/min from 10 to 800 °C under a constant purge flow rate of nitrogen.

2.8. Mechanical Test. *2.8.1. Compressive Test.* Compressive tests were performed according to ASTM standard D695-10, using cylindrical shaped 1-by-2 cm specimens. Scaffold compressive stress−strain curves were measured at room temperature using a tensile tester (Instron, model 3365) with a 5 kN cell load at a crosshead speed of 1.3 mm/s. The compressive modulus was calculated by taking the slope of the initial linear portion of the stress−strain curve, while yield strength was calculated by intersecting a line parallel to the linear region beginning at 0.2% deformation.

2.8.2. Cyclic Load. Scaffolds were immersed in phosphate buffered saline (PBS) at 37 °C during 24, and then, the samples were tested under cyclic loading conditions. Samples were compressed and reverted toward the original length five times at a displacement rate of 5 mm/s. The lower limit was set to 10 kPa and upper limit to 35 kPa.

2.9. Contact Angle and Water Absorption. Contact angle was measured and was determined on a contact angle device (Drop Shape Analyzer DSA25S, KRUSS) controlled by ADVANCE software (KRUSS) on PU scaffold surfaces and porous nanogold/PU scaffolds. Contact angles on the polymer surfaces were measured by the sessile drop or static drop method at a temperature of 25 °C. Drops of 5 μL of different solvents, water, or ethylene glycol were deposited on the polymer surfaces.

Water absorption of the PU scaffolds and porous nanogold/PU scaffolds were measured by immersing the scaffold nanocomposites in distilled water for a predetermined time. The samples were then removed and excess water was removed with filter paper and subsequently weighed. The resulting weight is termed W_1. Finally, the samples were completely vacuum-dried and weighed again; this second weight is termed W_2. Water absorption was calculated according to the method described by Cai.[34]

2.10. In Vitro Degradation Assay. In vitro degradation of the samples was evaluated by recording the weight loss and changes in mechanical properties over time in PBS buffer solution at 67 °C. Each PU sample was cut into cylindrical shapes of 10 mm (height) by 15 mm (diameter) with the weight of about 170 mg. The samples were immersed in tubes with 10 mL PBS solution (pH = 7.4). The tubes were placed in a 67 °C water bath with gentle shake of approximately 80 rpm to accelerate the degradation rate. At each time point of week 1, 2, 3, and 4, four tubes of each kind of material were sampled, rinsed for 1 h by deionized water, and vacuum-dried for 3 days before analysis of weight loss. The weight remaining was calculated as

DOI: 10.1021/acsami.8b02347
ACS Appl. Mater. Interfaces 2018, 10, 13361−13372

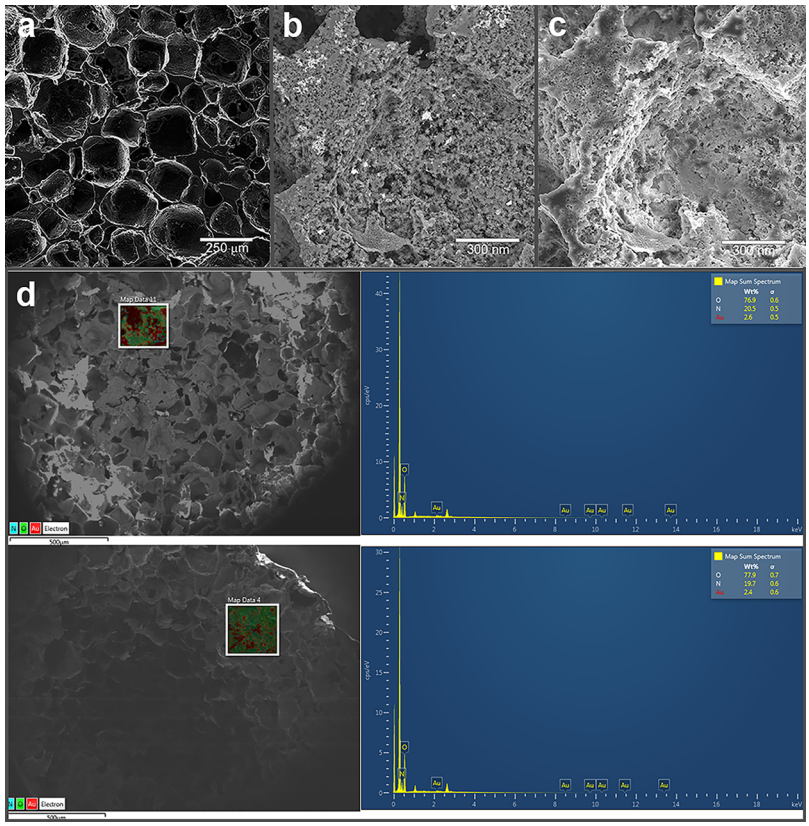

Figure 2. (a) SEM image of porous nanogold/PU scaffolds, (b) SEM image of AuNPs incorporated into the PU scaffold in back scattering mode, (c) secondary electrons mode, and (d) EDS-Au mapping for two regions of porous scaffold sample with its EDS spectrum respective.

$$\text{Weight remaining}\ (\%) = 100 \times W_2/W_1$$

where W_1 and W_2 are the weights of samples before and after degradation assay, respectively.[35]

2.11. Antibacterial Assessment. *2.11.1. Bacterial Viability.* Antibacterial capability was assessed against *S. epidermidis* and *Klebsiella* spp. Bacteria were grown in Mueller Hinton culture broth at 37 °C for 16 h. The resulting culture was then transferred to a fresh medium and standardized to 10^6 CFU/mL by measuring optical density at 600 nm. One drop of this solution was deposited on the surface of the porous nanocomposites 1 cm in diameter and then incubated for 24 h. Samples were washed with 10 mL of a solution containing 0.88 wt % NaCl and 1 wt % Tween 80. This was done to remove the bacteria incubated on the surface of the nanocomposite. Subsequently, 50 μL of the solution with entrained bacteria was transferred to a nutrient Mueller Hinton agar medium and incubated for 16 h at 37 °C. Colonies were counted after incubation. The experiments were repeated five times.

2.11.2. Scanning Electron Microscopy. Porous samples were inoculated with 400 μL of bacterial suspension and incubated at 37 °C for 16 h. The samples were then rinsed twice with 0.01 M of sodium cacodylate/0.15 M NaCl buffer at pH 7.0 for 15 min and fixed with 1% glutaraldehyde in 0.01 M of sodium cacodylate/0.15 M NaCl buffer at pH 7.0 for 2 h at room temperature. The samples were then rinsed twice in 0.01 M of sodium cacodylate/0.15 M NaCl buffer at pH 7.0 for 15 min. Finally, the samples were dehydrated in ascending grades of ethanol (30, 50, 70, 80, 90, and 100%), after which they were coated with a thin film of Pt/Pd.

2.12. In Vitro Cytotoxicity Assay. T10 1/2 fibroblasts were cultured in Dulbecco's modified Eagle's medium (DMEM; Gibco, Life Technologies) supplemented with 100 U/mL of penicillin, 100 μg/mL of streptomycin (Gibco, Life Technologies, USA), and 10% (v/v) fetal bovine serum (Biological, USA) at 37 °C in a 5% CO_2 atmosphere. Cells were seeded at a density of 5000 cells per well and left for 1 h until the cells adhered to the 96-well plate. Then, PU and PU−Au scaffolds were then immersed in 1 mL of DMEM for 24 h, and finally, samples were placed directly on top of the cell monolayer and covered by cell culture medium for 1, 3, and 5 days. The cell viability and morphology was determined using MTS reduction assay or calcein-AM dye. MTS was bioreduced by cells into a formazan product that is soluble in the cell culture medium. The absorbance of the formazan was determined by a colorimetric end point kit, according to the manufacturer's instructions (Promega, USA). Fibroblast viability (mean ± SEM) is expressed as the percentage of live cells relative to control cultures. When using the calcein-AM dye, the cells were incubated with PU and PU−Au 0.64 for 24 h. Then, the culture medium was removed, and the cells were gently washed three times with PBS. Cells were then incubated at room temperature for 10 min with PBS containing 2 mM calcein-AM ester and washed three times with PBS to allow complete dye de-esterification. Finally, randomly chosen fields were examined per culture well per experimental condition.

3. RESULTS AND DISCUSSION

3.1. Morphological Characterization of the AuNPs and Porous Nanogold/PU Scaffolds. Figure 1a shows the TEM image of AuNPs. Highly monodisperse AuNPs have a sea urchin-shaped morphology. The histogram of size distribution (Figure 1b) measured by the dynamic light scattering technique reveals a mean nanoparticle diameter of 33 nm. The morphology of nanoparticles is related to the orientation of the gelatin chains on silver seeds. As the working pH used in the synthesis was lower than the isoelectric point, the gelatin was positively charged, which allowed its adsorption on silver seeds negatively charged by the citrate, preferentially adsorbing on the {100} crystal faces.[32] This behavior promotes the formation of the sea urchin-shaped AuNPs. To evaluate the purity of the AuNPs, X-ray diffraction (XRD) analysis and EDS

DOI: 10.1021/acsami.8b02347
ACS Appl. Mater. Interfaces 2018, 10, 13361−13372

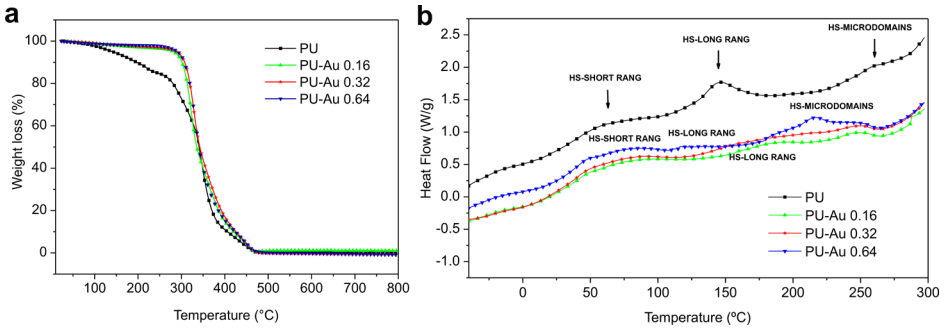

Figure 3. (a) TGA curves of the PU scaffold and porous nanogold/PU scaffolds with different quantities of AuNPs; (b) DSC thermograms of the PU scaffold and porous nanogold/PU scaffolds with different quantities of AuNPs.

were performed to observe signals associated with the presence of nanoparticles or other species. The diffractogram in Figure 1c shows the typical diffraction peaks at 38.5°; 44.4°; 64.7°; 77.4°, and 82.2°, which correspond to (111), (200), (220), (311), and (222) Bragg's reflection, respectively, based on the cubic structure centered on the faces.[36] No additional signals are observed in the diffractogram, indicating the purity of the nanoparticles. EDS spectrum in Figure 1d displays the purity and chemical composition of AuNPs showing strong signals for gold at 2.12 and 9.71 keV. The other signals correspond to oxygen, nitrogen, and carbon present in gelatin. The presence of copper is due to the copper grid used as support for the nanoparticles.

The sea urchin-shaped AuNPs were incorporated into the PU at 80 °C. To verify the successful preparation of PU, the ^{1}H NMR spectrum was obtained. Figure S1 (Supporting Information) shows the ^{1}H NMR spectrum of PU with the typical resonance signals. Each signal is associated with the corresponding proton of the proposed structure. Signals at 4.04−4.08 ppm (t-Hi,k,e), at 3.14−3.16 ppm (d-Hf), at 2.29−2.31 ppm (m-Ha), at 1.61−1.69 ppm (m-Hb,d,j), at 1.44−1.49 ppm (m-Hg,h), and 1.24−1.39 ppm (m-Hc) match with the corresponding protons.[37] The Fourier transform infrared spectroscopy (FT-IR) spectrum of the PU is shown in Figure S2 (Supporting Information). The absence of NCO stretching vibration at 2270 cm^{-1} indicates the completion of the reaction of synthetized PU. A characteristic band of urethane absorbance at 3334 cm^{-1} is attributed to H-bonded −NH groups.[38] The peaks at 2925 and 2865 cm^{-1} are associated with the asymmetric and symmetric $-CH_2$ groups and absorbance at 1445 and 1355 cm^{-1} corresponding to the other modes of $-CH_2$ deformations. The peak around 1717 cm^{-1} is assigned to stretching vibration of free C═O groups. The C═O group involved in hydrogen bonding absorbs at 1665 cm^{-1}. The peak of urethane ether linkage absorbs at 1125 and 1140 cm^{-1}.

The porous structure was achieved by the salt leaching technique, resulting in gold−PU scaffolds with a porosity of 82−85%. Figure 3 shows the SEM images of porous nanogold/PU scaffolds. The porous microstructure of the nanocomposites (Figure 2a) consists of interconnected open micropores with diameters between 50 and 300 μm. The presence of AuNPs (bright areas) in the PU is shown in the backscattered electron image (Figure 2b). The same region in secondary electron mode is shown in Figure 2c. The nanoparticles are larger than those observed in the TEM image in Figure 1a, indicating aggregation and formation of clusters when they are incorporated into the polymer. The mean agglomerate size of the particles was 320 nm in diameter.

Figure 2d shows a representative EDS map of elemental distribution of two different regions of a scaffold sample, where a red color indicates the presence of gold. For each region, the respective EDS spectrum is showed. In both cases, the spectra reveal that the main composition of the sample is nitrogen and oxygen, both present in the PU, while carbon was not analyzed because the sample was covered with this element. The gold signal at 2.13 eV associated to AuNPs[39] is small because of low concentration of these nanoparticles. The table inset in the spectra shows similar atomic percentages which indicate a chemical composition uniform inside the sample.[40]

3.2. Thermal Analysis of Porous Nanogold/PU Scaffolds. Thermal degradation of porous PU scaffolds containing different quantities of AuNPs was also evaluated by TGA. Figure 3a shows thermograms for PU, PU−Au 0.16, PU−Au 0.32, and PU−Au 0.64. Weight loss at 250−350 °C is attributed to the dissociation of urethane bonds to form isocyanates, alcohol, amines, and CO_2.[41] In general, the degradation-onset temperature increased with the addition of AuNPs. As well, the weight loss at 290 °C decreased with the quantity of AuNPs. These results indicate that thermal resistance is enhanced by the addition of adding AuNPs.

The PU structure is composed of alternating soft and hard segments. The soft segments have a low glass transition temperature (T_g) and form a continuous flexible matrix. The hard segments have high melting points (T_m) and tend to self-assemble into domains through physical cross-linking.[42] PUs generally have several thermal transitions, corresponding to the microstructure of the hard segments. It is possible to observe by differential scanning calorimetry (DSC) thermograms the melting points of three hard segments at 60−80, 120−190, and over 200 °C, associated with short-range, long-range, and microcrystalline ordering of hard segment domains.[43] In our case, the thermograms in Figure 3b show three melting peaks for neat PU at 30−95, 125−175, and 245−280 °C, for PU−Au 0.16 and PU−Au 0.32 at 25−120, 130−225, and 230−280 °C, while PU−Au 0.64 at 25−100, 110−160, and 160−280 °C, respectively. This behavior suggests that the presence of 0.64 wt % of AuNPs change significantly the microstructure of the PU, with an increase in microcrystalline hard segments and decrease in long-range hard segments. Hsu et al.[44] also studied the effect of AuNPs on the PU morphology, although the changes in the structure obtained in their work were revealed by atomic force microscopy; the thermograms obtained by DSC only shows one melting peak (at 46.9−48.2 °C). It is likely that the morphological changes obtained by Hsu et al. were only short-range because of the small quantity of AuNPs incorporated into the polymer. The change in the crystalline of the polymer due

DOI: 10.1021/acsami.8b02347
ACS Appl. Mater. Interfaces 2018, 10, 13361−13372

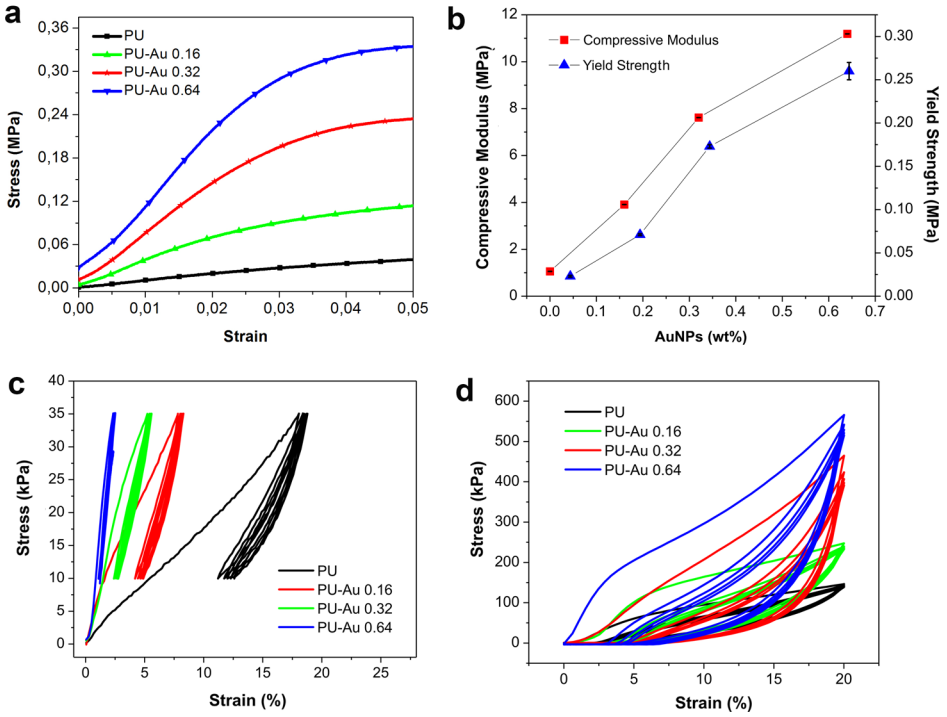

Figure 4. (a) Stress−strain curves of PU and porous nanogold/PU scaffolds, (b) compressive modulus and yield strength of PU and porous nanogold/PU scaffolds with different quantities of nanoparticles, and (c) cyclic behavior of PU and PU−AuNPs under wet and (d) dry conditions.

to the effect of the AuNPs was confirmed by XRD. The XRD patterns of PU and PU−Au 0.64 are depicted in Figure S3 (Supporting Information). Both samples show a peak at 2θ = 20°. In both cases, the broadened peak might be due to the presence of small crystalline structures or diffraction from crystals of PCL, whereas the sharp peak at 2θ = 24.5° is related to the formation of crystalline structures in hard segments.[38] The peaks in the diffractogram of PU−Au 0.64 are intensified and narrowed, which would indicate an increase in crystallinity because of the presence of AuNPs. The broad peaks at 2θ = 38−39° in PU−Au 0.64 correspond to the crystal faces of (111) and (200) of zero-valent gold in the face-centered cubic structure, confirming the presence of AuNPs.

3.3. Mechanical Behavior. Mechanical tests (compressive modulus and yield strength) evaluated the effect of the quantity of AuNPs on the stiffness of the PU. Compressive modulus and yield strength were evaluated from the stress−strain curves (Figure 4a). The yield strength values were computed by using the offset-yield point at 0.2% of strain. Figure 4b shows compressive modulus values of 1.057 ± 0.001, 3.909 ± 0.001, 7.617 ± 0.001, and 11.182 ± 0.001 MPa and yield strength (σ_y) values of (2.3 ± 0.1) × 10^{-2}, (7.1 ± 0.1) × 10^{-2}, (1.8 ± 0.02) × 10^{-1}, and (2.6 ± 0.1) × 10^{-1} MPa for nanocomposites with 0, 0.16, 0.32, and 0.64 wt % of AuNPs, respectively. These results demonstrate a relationship between the stiffness of porous nanogold/PU scaffolds and the quantity of AuNPs. Thus, an increased stiffness could be associated to changes in the microstructure of the hard segments of the PU because of increase of AuNPs (Figure 3b). The thermograms show a slight increase in the area under the curve of endotherms associated with the microcrystalline domains of hard segments for the nanocomposites with larger quantities of AuNPs (0.32 and 0.64 wt %) relative to PU without AuNPs. This suggests that AuNPs act as nucleation centers that promote the formation of microcrystalline domains of hard segments. The primary driving force for hard domain aggregation (microcrystalline domains) is the strong intermolecular interaction between urethane units that are capable of forming interurethane hydrogen bonds.[42] Considering that AuNPs are stabilized by gelatin, it is probable that amide groups in the gelatin form hydrogen bonds with the urethane groups of the polymer. This interaction facilitates the hard segments to orient themselves around the nanoparticles by promoting the formation of microcrystalline microdomains. He et al.[42] argued that if the more polar urea linkages are incorporated into the molecular backbone, the order degree of the hard domain structure will increase considerably because of the formation of bidentate hydrogen bonding. Given that microcrystalline domains act as the reinforcing filler of the polymer, an increase in these hard domains improves the stiffness of the nanocomposite.[45]

An important point in the work of Hsu et al.[44] is that the difference in the compression module of the PU with and without nanoparticles did not exceed 60%, while in our case the value of the module for PU−Au 0.64 was 1000% greater than that for the PU without nanoparticles (10 times as high). It is important to compare the results because these clearly confirm the effect of the quantity of AuNPs on the structural changes of PU. In future studies, it would be interesting to determine the critical concentration range associated with this transition. Meanwhile, considering that the aim of our work is to develop a material with applications in soft tissue implants, the stiffness value obtained with 0.64 wt % of AuNPs is adequate for our studies. The values of the Young's modulus of the scaffolds are near to the mechanical properties of the human meniscus or hyaline cartilage, where the compression modulus is approximately 0.22 and 8.4−15.3 MPa, respectively.[8]

Considering that the daily activities of living beings involve repetitive effort of the tissues, the cyclic behavior of the scaffolds was evaluated. The cyclic behavior of PU and PU−AuNPs under wet conditions is shown in Figure 4c. Different

DOI: 10.1021/acsami.8b02347
ACS Appl. Mater. Interfaces 2018, 10, 13361−13372

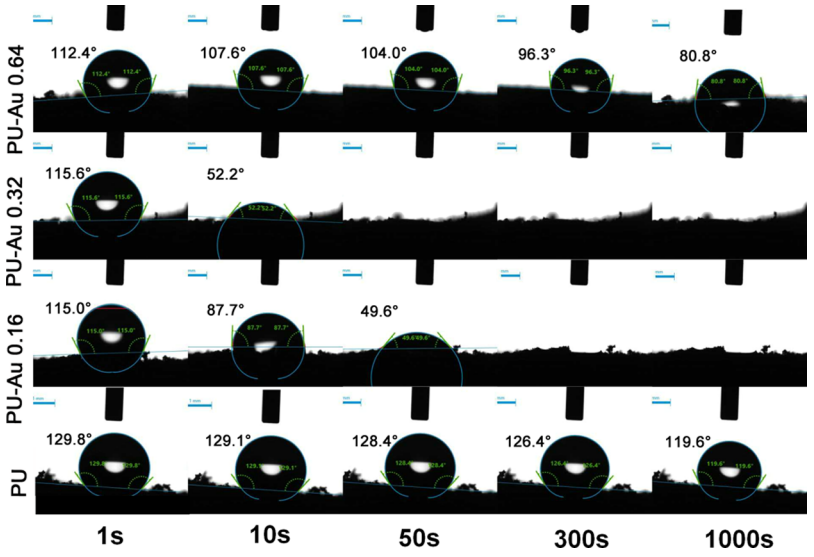

Figure 5. Profiles of 5 μL water droplets on PU, PU−Au 0.16, PU−Au 0.32, and PU−Au 0.64, showing contact angle values as a function of time.

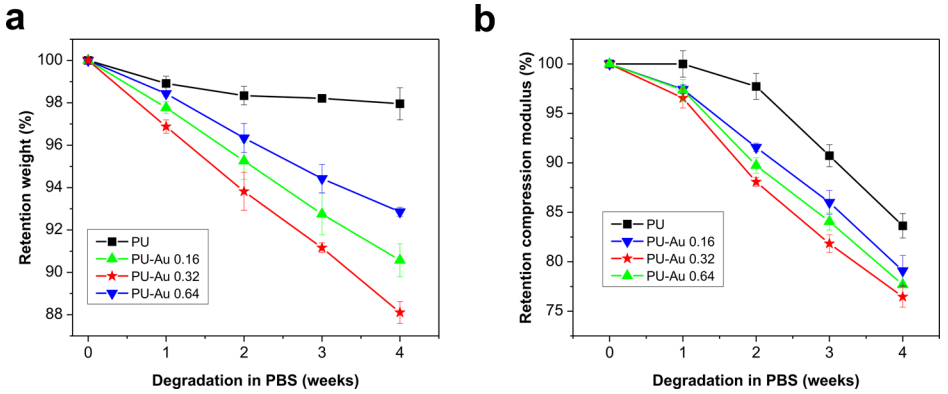

Figure 6. Degradation behavior of PU, PU−Au 0.16, PU−Au 0.32, and PU−Au 0.64. (a) Average retention weight as a function of degradation in PBS during 4 weeks and (b) average retention compression modulus as a function of degradation in PBS during 4 weeks.

deformation ranges were observed when the samples were subjected to a constant stress of 10−35 kPa. The PU sample reached a maximum deformation of 16% and a large hysteresis loop in each cycle. It is possible to observe that as the quantity of nanoparticles increases, the deformation decreases. Thus, PU−AuNPs 0.64 reached a maximum deformation of 2% with a lower hysteresis loop. However, for the dry tests (Figure 4d) the samples showed no measurable deformation when subjected to a stress of 10−35 kPa. Given the difference in stiffness with respect to the wet samples, a large stress was applied to the samples, sufficient to reach a 20% deformation. The maximum stress required for PU was 130 kPa, which increased with the increase in nanoparticles as seen in Figure 4b. For PU−AuNPs 0.64, the maximum stress required was 560 kPa, 5 times higher than that of PU.

3.4. Contact Angle Measurements and Water Absorption. Figure 5 shows the contact angle profiles obtained for PU, PU−Au 0.16, PU−Au 0.32, and PU−Au 0.64 as a function of time. It can be observed that the contact angles of PU−Au 0.32 and PU−Au 0.16 are the lowest, indicating a significant reduction of the hydrophobic character of the nanocomposite, whereas PU−Au 0.64 shows a larger value of the contact angle. We believe that the presence of nanoparticles stabilized with gelatin play an important role in the hydrophilic/hydrophobic character of the samples. Although gelatin has a relative hydrophilic character, on solid surfaces this could be influenced by the orientation of the gelatin chains in the polymer. A typical structure of gelatin has a sequence Ala-Gly-Pro-Arg-Gly-Glu-4Hyp-Gly-Pro,[46] containing hydrophobic domains associated to the presence of alanine (Ala), glycine (Gly), and proline (Pro). On the basis of this assumption, we believe that the sample with the highest quantity of nanoparticles (PU−Au 0.64) contains a larger number of gelatin chains whose orientation exposes the hydrophobic domains toward the polymer or the surface, whereas hydrophilic domains interact with nanoparticles, giving a more hydrophobic character to the sample. Figure S4 (Supporting Information) shows the percentage of water absorbed by each sample. For all nanocomposites, the amount of water absorbed is greater than the weight of the samples (absorption values are >100%). The water absorption behavior is consistent with the change of the contact angle in the time shown in Figure 5, where the maximum percentage of water absorbed at 1 h was 615 ± 2.65% for PU−Au 0.32, followed by PU−Au 0.16 with 432.5 ± 0.95%, PU−Au 0.64 with 286 ± 4.11%, and finally PU with 28.7 ± 1.14%. This critical maximum absorption concentration for PU−Au 0.32 could be influenced by the presence of AuNPs and built-in gelatin, particularly related to the orientation of the hydrophobic domains of gelatin, as explained for the contact angle behavior.

DOI: 10.1021/acsami.8b02347
ACS Appl. Mater. Interfaces 2018, 10, 13361−13372

3.5. In Vitro Degradation Assay. In vitro degradation assay was performed by weight loss (Figure 6a) and compression module (Figure 6b) measurements of the samples immersed in PBS buffer. Figure 6a shows the degradation curves as a function of the weight retained for PU, PU−Au 0.16, PU−Au 0.32, and PU−Au 0.64 for 1, 2, 3, and 4 weeks. The scaffolds show a progressive weight loss during the 4 weeks varying between 1.1 and 2.0% for PU, 2.2−9.4% for PU−Au 0.16, 3.1−11.9% for PU−Au 0.32, and 1.6−7.1% for PU−Au 0.64. The degradation rate for PU−Au 0.32 is higher than that for the rest of the samples. The increase in degradation follows the same behavior as observed in the water absorption curve. It is likely that the increase in the hydrophilic character due to the effect of nanoparticles accelerates polymer degradation. This is based on the fact that the increase in hydrophilicity promotes the incorporation of water molecules inside the internal structure of the polymer and therefore the hydrolytic degradation. On the other hand, it is known that the interaction between the polymer chains resist the attack of the water molecules on the ester group. Therefore, the presence of hard segment microdoamins would act as a tortuous path for the diffusion of water.[47] In this way, as the increase in AuNPs promotes the formation of microcrystalline domains, degradation of PU−Au 0.64 is expected to be slower than that of PU−Au 0.16 and PU−Au 0.32.

3.6. Antibacterial Properties. The antibacterial activity of porous nanogold/PU scaffolds was evaluated against *Klebsiella* spp. and *S. epidermidis* by the viable cell count method and SEM images.

Figure 7 shows the colony forming units (CFUs) of *S. epidermidis* and *Klebsiella* spp. on the agar plates. In both cases, the number of colonies decreased when the AuNP concentrations increased. The viability of *Klebsiella* spp. and *S. epidermidis* incubated on nanocomposites with 0.32 wt % of AuNPs was less than 10%. No viable CFUs of *Klebsiella* spp. and *S. epidermidis* were observed at 0.64 wt % of AuNPs, achieving over 99.99% reduction of the colonies (Figure 7i). These results demonstrate the antibacterial efficacy of porous nanogold/PU scaffolds.

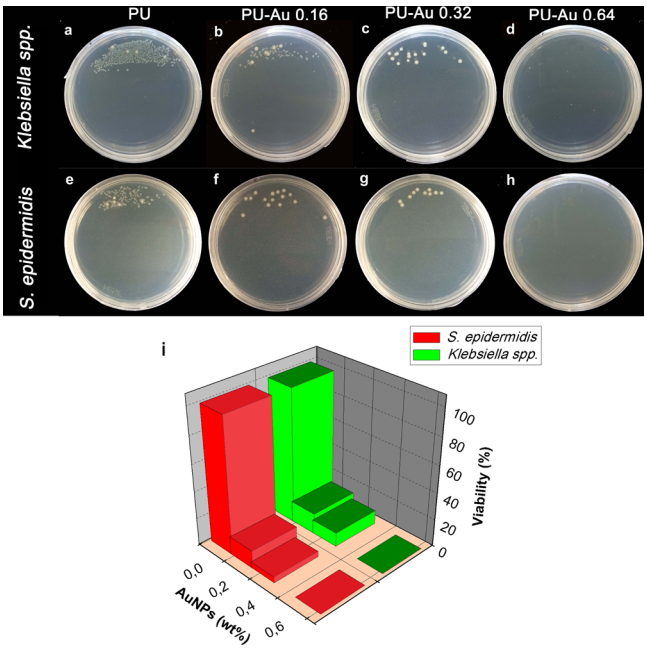

Figure 7. Photograph of colonies of *Klebsiella* spp. (top row) and *S. epidermidis* (bottom row) on agar plate for (a,e) PU, (b,f) PU−Au 0.16, (c,g) PU−Au 0.32, and (d,h) PU−Au 0.64. (i) Percentage of viability of *S. epidermidis* and *Klebsiella* spp. as a function of the quantity of AuNPs.

SEM images of the surface PU and porous nanogold/PU scaffolds were obtained after 24 h of incubation to determine the presence or absence of *Klebsiella* spp. and *S. epidermidis* (Figures 8 and 9). A large population of bacteria can be observed within and outside the pores on the PU surface.

It can be seen in the images that the population of *S. epidermidis* on PU is less abundant than that of *Klebsiella* spp., even though both cultures were standardized to 10^6 CFU. This suggests that the PU slightly inhibits the adhesion of *S. epidermidis*. Studies have shown that *S. epidermidis* adheres less to hydrophilic PU than to hydrophobic surfaces.[48,49] In our case, it is likely that the presence of AuNPs and gelatin used as a capping agent of AuNPs provided a more hydrophilic character to the polymer, which contributed to inhibiting adhesion of *S. epidermidis*. In general, bacteria adhere preferentially on hydrophobic surfaces because of a thermodynamic stability. Rosenberg and Kjelleberg argue that most bacteria contain hydrophobic surface components, which can be important in adhesion to other surfaces because hydrophobic interactions tend to increase with the increasingly nonpolar nature of one or both of the surfaces involved.[50] Given that increasing the presence of AuNPs stabilized with gelatin in PU enhances the hydrophilicity of the polymer, we believe that the change from a hydrophobic to hydrophilic character also contributes to the antibacterial activity of porous nanogold/PU scaffolds.

It is interesting to consider that the quantity of AuNPs in polymer is lower than those of other antibacterial metal−nanocomposites. Some studies have shown silver−PU nanoparticles require up to 10 wt % of silver nanoparticles to reduce *E. coli* and *S. typhimurium* by 99.9%.[51] Similarly, nanocomposites based on PU and copper nanoparticles need between 5 and 10 wt % of nanoparticles to inhibit the growth of *E. coli* and *B. subtilis*.[52] It is likely that the scaffolds require a lower amount of AuNPs because of the kind of antibacterial and antibiofilm effects that are carried out and the characteristics of this material. To understand the possible phenomena that could be carried out and clarify if there is an effect of repulsion or attraction between the surface of the scaffolds and the bacteria, the Z potential of the nanoparticles, PU, and PU−AuNPs were measured. The values so obtained were −6.85, −0.25, and −15.1 mV, respectively. On the basis of these results, we believe that the antibiofilm effect is mainly due to a phenomenon of repulsion. Considering that the Z potential of a bacterium lies between −17 and −48 mV approximately,[53] the greater repulsion effect will be observed in PU−AuNPs, while the weak negative charge of PU will favor the adhesion of the bacteria, as shown in Figures 8 and 9. On the other hand, according to what was observed in the bacterial viability tests, the reduction of bacterial colonies for PU−Au 0.64 is 99.9% (Figure 7), which indicates that the scaffolds induce the death of the bacterium. It is probably that the bacterial death is associated to a bactericidal mechanism where the Au^{3+} ions penetrate the membrane and the cell wall, generating their destabilization.[54,55] This hypothesis is based on inductively coupled plasma (ICP) analyses performed to PU−AuNP immersion media obtaining a maximum value of 0.017 mg/g of gold released. In our case, the sea urchin-shaped morphology

DOI: 10.1021/acsami.8b02347
ACS Appl. Mater. Interfaces 2018, 10, 13361−13372

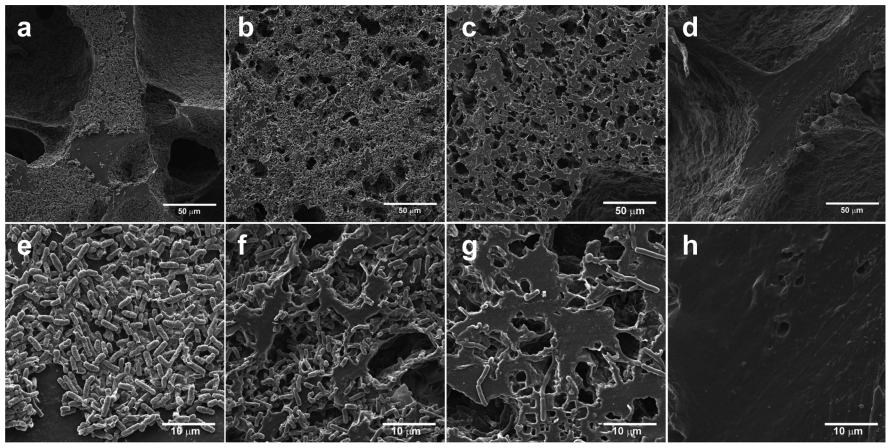

Figure 8. *Klebsiella* spp. incubated for 24 h on (a,e) PU, (b,f) PU−Au 0.16, (c,g) PU−Au 0.32, and (d,h) PU−Au 0.64.

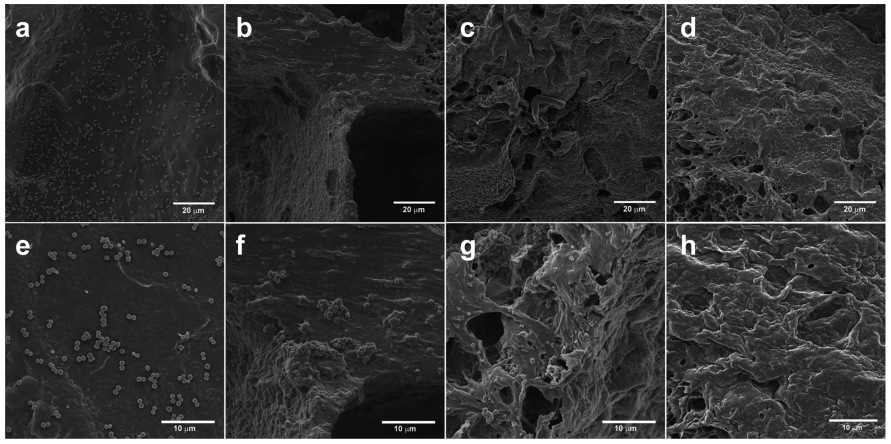

Figure 9. *S. epidermidis* incubated for 24 h on (a,e) PU, (b,f) PU−Au 0.16, (c,g) PU−Au 0.32, and (d,h) PU−Au 0.64.

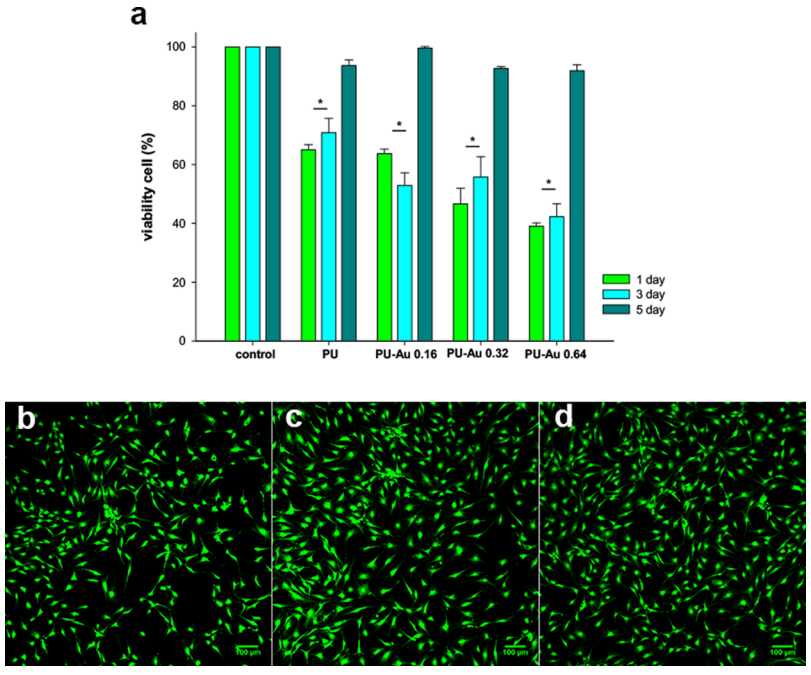

Figure 10. (a) Test of T10 1/2 fibroblast cell viability exposed to PU, PU−Au 0.16, PU−Au 0.32, and PU−Au 0.64 scaffolds for 1, 3, and 5 days. The results are expressed as percentage of live cells relative to untreated cells (control). Values represent the mean ± SEM of three independent experiments, in triplicate, $*p \leq 0.05$. T10 1/2 fibroblast morphologies and viability loaded with calcein-AM were visualized by confocal microscopy. Representative images of fibroblast control (b), exposed to PU−Au (c) and PU−Au 0.64 (d) scaffolds for 24 h. Scale bar, 100 μm.

DOI: 10.1021/acsami.8b02347
ACS Appl. Mater. Interfaces 2018, 10, 13361−13372

of nanoparticles may increase the quantity of ions released and thus improve their antibacterial activity associated with a larger exposed surface compared with gold nanospheres or nanorods.

Some authors have argued that the antibacterial effect of AuNPs is the result of electrostatic attraction of the positively charged nanoparticles and the negatively charged cell surfaces. Other studies have indicated that cells can approach the substratum, followed by conformational changes in the polymer surfaces that lead to other functional groups approaching the surface for the formation of short-range attractive polymeric interactions.[56] However, the Z potential values obtained in our work demonstrate that AuNPs present a repulsion effect, which enhanced when AuNPs are incorporated into the polymer.

In summary, we believe that the possible effects of porous nanogold/PU scaffolds against *S. epidermidis* and *Klebsiella* spp. are: electrostatic repulsion, release of Au^{3+} ions as a bactericidal agent, and unfavorable surface energy for adhesion (hydrophilicity). These could act simultaneously by enhancing the antibiofilm/antibacterial capacity of the scaffolds.

3.7. Cytotoxic Assays. Test of T10 1/2 fibroblast cell viability was carried out to assess the effect of PU and PU−Au scaffolds on fibroblast cell viability. The cytotoxicity assays were evaluated after 1, 3, and 5 days of exposure to scaffolds. The percentages of cell viability relative to controls shown in Figure 10a reveal that the scaffolds incubated have a reduction of 30% in the cell viability for PU and PU−Au 0.16 and 50% for PU−Au 0.32 and PU−Au 0.64 after 1 and 3 day of exposure to scaffolds, which can be considered as a slight and moderate cytotoxicity respectively.[57] However, this moderate cytotoxicity was reverted at 5 day of exposure, where percentages of viability reached almost 100%, hence not affecting the cell viability. Therefore, the moderate cytotoxicity induced for PU and PU−Au was transient, restoring the proliferative status of fibroblast cells as well as viability. To confirm morphology and adhesion in live fibroblasts after incubation of cultures for 24 h with PU scaffolds. The fibroblast cells were loaded with calcein-AM, and live cells were identified by their green calcein fluorescence. The confocal microscopy images compared with the control (Figure 10b) indicate that the live fibroblast cells exposed to PU (Figure 10c) and PU−Au 0.64 (Figure 10d) scaffolds did not produce substantial changes in morphology and adhesion capacity of fibroblast cells. These results are consistent with those reported by Barrioni,[58] who also synthesized PU-based PCL and HMDI monomers.

In in vivo assays, the toxic effects of AuNPs generally depend on their size, charge, and surface hydrophobicity.[59] Regarding size, it has been observed that small nanoparticles (15 nm) can permeate the skin and intestine,[60] whereas the larger nanoparticles (250 nm) remain in the blood, liver, and spleen.[61] Nanoparticles of intermediate size (50 nm) are able to overcome the blood−brain barrier.[62] On the other hand, it has been observed that functionalized nanoparticles with amphiphilic chains decrease the phagocytosis of cells in the liver, allowing a greater circulation time in the blood. In relation to surface loading, it has been shown that negatively charged nanoparticles remain longer in the liver and spleen, whereas positively charged nanoparticles can cause little damage to the peripheral blood system.[63] Other in vivo studies in rats have shown that the nanoparticles of smaller sizes (3 and 5 nm) and larger sizes (50 and 100 nm) are not toxic at a dose of 8 mg gold/kg, whereas the nanoparticles of intermediate size range of 8−37 nm had lethal effects in mice, inducing loss of appetite, weight loss, change in skin color, and a shorter half-life.[64]

Considering these antecedents, in our study, we quantified by ICP spectrometry, the amount of nanoparticles that could be released from the nanocomposite, obtaining values of 0.017 mg per g of sample after 30 days of immersion. Estimating that a meniscus implant has a mass of 5 g, the amount of AuNPs released would be 0.085 mg, and if an adult man weighs 80 kg, the dose of nanoparticles present in the body would be 1.06×10^{-3} mg/kg, whose value is much lower than that used in the in vivo tests, which would allow us to rule out its toxicity.

4. CONCLUSIONS

Developing biomaterials that solve the current problems in the use of medical implants is a major challenge. In this work, we have presented the synthesis, elaboration, and evaluation of the mechanical, thermal, cytotoxic, and antibiofilm properties of a biomaterial based on PU and AuNPs stabilized with gelatin. The results show that small increase in the quantity of AuNPs enhances antibiofilm activity of the nanocomposite, inhibiting 99.99% of *Klebsiella* spp. and *S. epidermidis*, both bacteria associated with implant infections. Cytotoxicity assays revealed that porous nanogold/PU scaffolds do not exhibit toxic effects on fibroblast cells, with nearly 100% viability to 5 days of incubation, in addition the morphology and adhesion capability cells is not different to untreated cells. The incorporation of AuNPs also changed the microcrystalline structure of the hard segments of the PU, increasing by up to 10 times the values of the compressive modulus and strength, while improving the thermal properties of the PU. These results demonstrate that porous nanogold/PU scaffolds are an ideal biomaterial for soft tissue implants.

■ ASSOCIATED CONTENT

Supporting Information

The Supporting Information is available free of charge on the ACS Publications website at DOI: 10.1021/acsami.8b02347.

Characterization of PU by ^{1}H NMR, FT-IR, XRD of PU and PU−AuNPs; water absorption; antibacterial assays using PU and PU−AuNPs films; and experimental data of ICP analysis and zeta potential (PDF)

■ AUTHOR INFORMATION

Corresponding Authors

*E-mail: laura.tamayo@uautonoma.cl (L.T.).
*E-mail: maurzua@uchile.cl (M.U.).

ORCID

L. Tamayo: 0000-0003-1159-5305
M. Urzúa: 0000-0002-1894-2384

Author Contributions

The manuscript was written through contributions of all authors. All authors have given approval to the final version of the manuscript. L.T., D.A., A.L.R., M.J.K., M.I.A., M.P., M.L., M.U., and E.C. contributed equally.

Notes

The authors declare no competing financial interest.

■ ACKNOWLEDGMENTS

L.T. is grateful for funding from FONDECYT Iniciation grant 11160230, FONDECYT postdoctoral grant 3140099, and PAI-CONICYT 79170015. The authors also are grateful to CONICYT (grant ACT-1412). M.U. is grateful to FONDECYT Regular grant 1151221, M.I.A. acknowledges the financial

DOI: 10.1021/acsami.8b02347
ACS Appl. Mater. Interfaces 2018, 10, 13361−13372

support by FONDECYT Regular (1140226), and M.K. is grateful to Fondap 15130011.

REFERENCES

(1) Chen, Q.; Liang, S.; Thouas, G. A. Elastomeric biomaterials for tissue engineering. *Prog. Polym. Sci.* **2013**, *38*, 584−671.

(2) Leal-Egaña, A.; Scheibel, T. Silk-based materials for biomedical applications. *Biotechnol. Appl. Biochem.* **2010**, *55*, 155−167.

(3) Pérez-Tanoira, R.; Han, X.; Soininen, A.; Aarnisalo, A. A.; Tiainen, V.-M.; Eklund, K. K.; Esteban, J.; Kinnari, T. J. Competitive colonization of prosthetic surfaces by staphylococcus aureus and human cells. *J. Biomed. Mater. Res.* **2017**, *105*, 62−72.

(4) Flemming, H.-C.; Wingender, J.; Szewzyk, U.; Steinberg, P.; Rice, S. A.; Kjelleberg, S. Biofilms: an emergent form of bacterial life. *Nat. Rev. Microbiol.* **2016**, *14*, 563−575.

(5) Francolini, I.; Donelli, G. Prevention and control of biofilm-based medical-device-related infections. *FEMS Immunol. Med. Microbiol.* **2010**, *59*, 227−238.

(6) Dorozhkin, S. V. *Clinical Applications of Biomaterials: State-of-the-Art Progress, Trends, and Novel Approaches*; Kaur, G., Ed.; Springer International Publishing, 2017; Chapter 5, pp 123−226.

(7) Lai, J. H.; Levenston, M. E. Meniscus and cartilage exhibit distinct intra-tissue strain distributions under unconfined compression. *Osteoarthritis Cartilage* **2010**, *18*, 1291−1299.

(8) Almarza, A. J.; Athanasiou, K. A. Design characteristics for the tissue engineering of cartilaginous tissues. *Ann. Biomed. Eng.* **2004**, *32*, 2−17.

(9) Curley, C.; Hayes, J. C.; Rowan, N. J.; Kennedy, J. E. An evaluation of the thermal and mechanical properties of a salt-modified polyvinyl alcohol hydrogel for a knee meniscus application. *J. Mech. Behav. Biomed. Mater.* **2014**, *40*, 13−22.

(10) Yang, D.; Shao, H.; Guo, Z.; Lin, T.; Fan, L. Preparation and properties of biomedical porous titanium alloys by gel casting. *Biomed. Mater.* **2011**, *6*, 045010.

(11) Kuang, T.; Chen, F.; Chang, L.; Zhao, Y.; Fu, D.; Gong, X.; Peng, X. Facile preparation of open-cellular porous poly (l-lactic acid) scaffold by supercritical carbon dioxide foaming for potential tissue engineering applications. *Chem. Eng.* **2017**, *307*, 1017−1025.

(12) Kim, H. Y.; Kim, H. N.; Lee, S. J.; Song, J. E.; Kwon, S. Y.; Chung, J. W.; Khang, G. Effect of pore sizes of PLGA scaffolds on mechanical properties and cell behaviour for nucleus pulposus regeneration in vivo. *J. Regen. Med. Tissue Eng.* **2017**, *11*, 44−57.

(13) Thadavirul, N.; Pavasant, P.; Supaphol, P. Development of polycaprolactone porous scaffolds by combining solvent casting, particulate leaching, and polymer leaching techniques for bone tissue engineering. *J. Biomed. Mater. Res.* **2014**, *102*, 3379−3392.

(14) Teo, A. J. T.; Mishra, A.; Park, I.; Kim, Y.-J.; Park, W.-T.; Yoon, Y.-J. Polymeric biomaterials for medical implants and devices. *ACS Biomater. Sci. Eng.* **2016**, *2*, 454−472.

(15) Hidalgo-Bastida, LA.; Barry, J. J. A.; Everitt, N. M.; Rose, F. R. A. J.; Buttery, L. D.; Hall, I. P.; Claycomb, W. C.; Shakesheff, K. M. Cell adhesion and mechanical properties of a flexible scaffold for cardiac tissue engineering. *Acta Biomater.* **2007**, *3*, 457−462.

(16) Gibson, L. J.; Ashby, F. A. *Cellular Solids*; Cambridge University Press, 1997.

(17) Li, K.; Zuo, Y.; Zou, Q.; Lin, L.; Wang, L.; Yang, B.; Hu, F.; Li, J.; Li, Y.; Li, J. Synthesis and Characterization of Injectable Nano-Hydroxyapatite/Polyurethane Composite Cement Effective Formulations for Management of Osteoporosis. *J. Nanosci. Nanotechnol.* **2016**, *16*, 12407−12417.

(18) Cohrs, N. H.; Schulz-Schönhagen, K.; Jenny, F.; Mohn, D.; Stark, W. J. Bioactive glass containing silicone composites for left ventricular assist device drivelines: role of Bioglass 45S5 particle size on mechanical properties and cytocompatibility. *J. Mater. Sci.* **2017**, *52*, 9023−9038.

(19) Malaki, M.; Hashemzadeh, Y.; Karevan, M. Effect of nano-silica on the mechanical properties of acrylic polyurethane coatings. *Prog. Org. Coat.* **2016**, *101*, 477−485.

(20) Mi, H.-Y.; Jing, X.; Salick, M. R.; Cordie, T. M.; Peng, X.-F.; Turng, L.-S. Morphology, mechanical properties, and mineralization of rigid thermoplastic polyurethane/hydroxyapatite scaffolds for bone tissue applications: effects of fabrication approaches and hydroxyapatite size. *J. Mater. Sci.* **2014**, *49*, 2324−2337.

(21) Pandey, S.; Jana, K. K.; Aswal, V. K.; Rana, D.; Maiti, P. Effect of nanoparticle on the mechanical and gas barrier properties of thermoplastic polyurethane. *Appl. Clay Sci.* **2017**, *146*, 468−474.

(22) de Villoria, R. G.; Miravete, A. Mechanical model to evaluate the effect of the dispersion in nanocomposites. *Acta Mater.* **2007**, *55*, 3025−3031.

(23) Raghavendra, G. M.; Jayaramudu, T.; Varaprasad, K.; Sadiku, R.; Ray, S. S.; Raju, K. M. Cellulose−polymer−Ag nanocomposite fibers for antibacterial fabrics/skin scaffolds. *Carbohydr. Polym.* **2013**, *93*, 553−560.

(24) Mei, L.; Lu, Z.; Zhang, X.; Li, C.; Jia, Y. Polymer-Ag nanocomposites with enhanced antimicrobial activity against bacterial infection. *ACS Appl. Mater. Interfaces* **2014**, *6*, 15813−15821.

(25) Yeroslavsky, G.; Lavi, R.; Alishaev, A.; Rahimipour, S. Sonochemically-produced metal-containing polydopamine nanoparticles and their antibacterial and antibiofilm activity. *Langmuir* **2016**, *32*, 5201−5212.

(26) Tamayo, L. A.; Zapata, P. A.; Vejar, N. D.; Azócar, M. I.; Gulppi, M. A.; Zhou, X.; Thompson, G. E.; Rabagliati, F. M.; Páez, M. A. Release of silver and copper nanoparticles from polyethylene nanocomposites and their penetration into Listeria monocytogenes. *Mater. Sci. Eng. C* **2014**, *40*, 24−31.

(27) Tamayo, L.; Azócar, M.; Kogan, M.; Riveros, A.; Páez, M. Copper-polymer nanocomposites: An excellent and cost-effective biocide for use on antibacterial surfaces. *Mater. Sci. Eng. C* **2016**, *69*, 1391−1409.

(28) Cui, Y.; Zhao, Y.; Tian, Y.; Zhang, W.; Lü, X.; Jiang, X. The molecular mechanism of action of bactericidal gold nanoparticles on Escherichia coli. *Biomaterials* **2012**, *33*, 2327−2333.

(29) Regiel-Futyra, A.; Kus-Liśkiewicz, M.; Sebastian, V.; Irusta, S.; Arruebo, M.; Stochel, G.; Kyzioł, A. Development of noncytotoxic chitosan−gold nanocomposites as efficient antibacterial materials. *ACS Appl. Mater. Interfaces* **2015**, *7*, 1087−1099.

(30) Ren, F.; Yesildag, C.; Zhang, Z.; Lensen, M. C. Surface Patterning of Gold Nanoparticles on PEG-Based Hydrogels to Control Cell Adhesion. *Polymers* **2017**, *9*, 154.

(31) Nagel, J. A.; Dickinson, R. B.; Cooper, S. L. Bacterial adhesion to polyurethane surfaces in the presence of pre-adsorbed high molecular weight kininogen. *J. Biomater. Sci. Polym. Ed.* **1996**, *7*, 769−780.

(32) Lu, L.; Ai, K.; Ozaki, Y. Environmentally friendly synthesis of highly monodisperse biocompatible gold nanoparticles with urchin-like shape. *Langmuir* **2008**, *24*, 1058−1063.

(33) Salehi, M.; Naseri Nosar, M.; Amani, A.; Azami, M.; Tavakol, S.; Ghanbari, H. Preparation of pure PLLA, pure chitosan, and PLLA/chitosan blend porous tissue engineering scaffolds by thermally induced phase separation method and evaluation of the corresponding mechanical and biological properties. *Int. J. Polym. Mater.* **2015**, *64*, 675−682.

(34) Cai, Q.; Yang, J.; Bei, J.; Wang, S. A novel porous cells scaffold made of polylactide−dextran blend by combining phase-separation and particle-leaching techniques. *Biomaterials* **2002**, *23*, 4483−4492.

(35) Guan, J.; Fujimoto, K. L.; Sacks, M. S.; Wagner, W. R. Preparation and characterization of highly porous, biodegradable polyurethane scaffolds for soft tissue applications. *Biomaterials* **2005**, *26*, 3961−3971.

(36) Narayanan, K. B.; Sakthivel, N. Coriander leaf mediated biosynthesis of gold nanoparticles. *Mater. Lett.* **2008**, *62*, 4588−4590.

(37) Zia, K. M.; Barikani, M.; Zuber, M.; Bhatti, I. A.; Sheikh, M. A. Molecular engineering of chitin based polyurethane elastomers. *Carbohydr. Polym.* **2008**, *74*, 149−158.

(38) Sadeghi, M.; Talakesh, M. M.; Ghalei, B.; Shafiei, M. Preparation, characterization and gas permeation properties of a

DOI: 10.1021/acsami.8b02347
ACS Appl. Mater. Interfaces 2018, 10, 13361−13372

polycaprolactone based polyurethane-silica nanocomposite membrane. *J. Membr. Sci.* **2013**, *427*, 21−29.
(39) Owens, D. E.; Eby, J. K.; Jian, Y.; Peppas, N. A. Temperature-responsive polymer−gold nanocomposites as intelligent therapeutic systems. *J. Biomed. Mater. Res.* **2007**, *83*, 692−695.
(40) Zhang, H.; Ding, W.; He, K.; Li, M. Synthesis and characterization of crystalline silicon carbide nanoribbons. *Nanoscale Res. Lett.* **2010**, *5*, 1264−1271.
(41) Petrović, Z. S. Polyurethanes from vegetable oils. *Polym. Rev.* **2008**, *48*, 109−155.
(42) He, Y.; Xie, D.; Zhang, X. The structure, microphase-separated morphology, and property of polyurethanes and polyureas. *J. Mater. Sci.* **2014**, *49*, 7339−7352.
(43) Van Bogart, J. WC.; Lilaonitkul, A.; Cooper, S. L. Morphology and properties of segmented copolymers. *Adv. Chem.* **1979**, *176*, 3−30.
(44) Hsu, S.-h.; Tang, C.-M.; Tseng, H.-J. Gold nanoparticles induce surface morphological transformation in polyurethane and affect the cellular response. *Biomacromolecules* **2007**, *9*, 241−248.
(45) Eceiza, A.; Martin, M. D.; de la Caba, K.; Kortaberria, G.; Gabilondo, N.; Corcuera, M. A.; Mondragon, I. Thermoplastic polyurethane elastomers based on polycarbonate diols with different soft segment molecular weight and chemical structure: mechanical and thermal properties. *Polym. Eng. Sci.* **2008**, *48*, 297−306.
(46) Alavijeh, R. Z.; Shokrollahi, P.; Barzin, J. A thermally and water activated shape memory gelatin physical hydrogel, with a gel point above the physiological temperature, for biomedical applications. *J. Mater. Chem. B* **2017**, *5*, 2302−2314.
(47) Mondal, S.; Martin, D. Hydrolytic degradation of segmented polyurethane copolymers for biomedical applications. *Polym. Degrad. Stab.* **2012**, *97*, 1553−1561.
(48) Jansen, B.; Goodman, L. P.; Ruiten, D. Bacterial adherence to hydrophilic polymer−coated polyurethane stents. *Gastrointest. Endosc.* **1993**, *39*, 670−673.
(49) Galliani, S.; Cremieux, A.; Van Der Auwera, P.; Viot, M. Influence of strain, biomaterial, proteins, and oncostatic chemotherapy on Staphylococcus epidermidis adhesion to intravascular catheters in vitro. *J. Lab. Clin. Med.* **1996**, *127*, 71−80.
(50) Rosenberg, M.; Kjelleberg, S. Hydrophobic Interactions: Role in Bacterial Adhesion. *Adv. Microb. Ecol.* **1986**, *9*, 353−393.
(51) Sheikh, F. A.; Barakat, N. A. M.; Kanjwal, M. A.; Chaudhari, A. A.; Jung, I.-H.; Lee, J. H.; Kim, H. Y. Electrospun antimicrobial polyurethane nanofibers containing silver nanoparticles for biotechnological applications. *Macromol. Res.* **2009**, *17*, 688−696.
(52) Sheikh, F. A.; Kanjwal, M. A.; Saran, S.; Chung, W.-J.; Kim, H. Polyurethane nanofibers containing copper nanoparticles as future materials. *Appl. Surf. Sci.* **2011**, *257*, 3020−3026.
(53) Soni, K. A.; Balasubramanian, A. K.; Beskok, A.; Pillai, S. D. Zeta potential of selected bacteria in drinking water when dead, starved, or exposed to minimal and rich culture media. *Curr. Microbiol.* **2008**, *56*, 93−97.
(54) Bindhu, M. R.; Umadevi, M. Antibacterial activities of green synthesized gold nanoparticles. *Mater. Lett.* **2014**, *120*, 122−125.
(55) Dasari, T. P. S.; Zhang, Y.; Yu, H. Antibacterial activity and cytotoxicity of gold (I) and (III) ions and gold nanoparticles. *Biochem. Pharmacol.* **2015**, *4*, 1−16.
(56) Habimana, O.; Semião, A. J. C.; Casey, E. The role of cell-surface interactions in bacterial initial adhesion and consequent biofilm formation on nanofiltration/reverse osmosis membranes. *J. Membr. Sci.* **2014**, *454*, 82−96.
(57) Lönnroth, E.-C. Toxicity of medical glove materials: a pilot study. *Int. J. Occup. Saf. Ergon.* **2005**, *11*, 131−139.
(58) Barrioni, B. R.; de Carvalho, S. M.; Oréfice, R. L.; de Oliveira, A. A. R.; de Magalhães Pereira, M. Synthesis and characterization of biodegradable polyurethane films based on HDI with hydrolyzable crosslinked bonds and a homogeneous structure for biomedical applications. *Mater. Sci. Eng. C* **2015**, *52*, 22−30.
(59) Zhang, G.; Yang, Z.; Lu, W.; Zhang, R.; Huang, Q.; Tian, M.; Li, L.; Liang, D.; Li, C. Influence of anchoring ligands and particle size on the colloidal stability and in vivo biodistribution of polyethylene glycol-coated gold nanoparticles in tumor-xenografted mice. *Biomaterials* **2009**, *30*, 1928−1936.
(60) Sonavane, G.; Tomoda, K.; Sano, A.; Ohshima, H.; Terada, H.; Makino, K. In vitro permeation of gold nanoparticles through rat skin and rat intestine: effect of particle size. *Colloids Surf., B* **2008**, *65*, 1−10.
(61) De Jong, W. H.; Hagens, W. I.; Krystek, P.; Burger, M. C.; Sips, A. J. A. M.; Geertsma, R. E. Particle size-dependent organ distribution of gold nanoparticles after intravenous administration. *Biomaterials* **2008**, *29*, 1912−1919.
(62) Sonavane, G.; Tomoda, K.; Makino, K. Biodistribution of colloidal gold nanoparticles after intravenous administration: effect of particle size. *Colloids Surf., B* **2008**, *66*, 274−280.
(63) Zhang, X.; Chen, J.; Yang, J.-Y.; Wang, H.; Shen, X.; Sun, Y.-M.; Meili, G.; Yang, J. Effects of surface charges of gold nanoclusters on long-term in vivo biodistribution, toxicity, and cancer radiation therapy. *Int. J. Nanomed.* **2016**, *11*, 3475−3485.
(64) Chen, Y.-S.; Hung, Y.-C.; Liau, I.; Huang, G. S. Assessment of the in vivo toxicity of gold nanoparticles. *Nanoscale Res. Lett.* **2009**, *4*, 858−864.

DOI: 10.1021/acsami.8b02347
ACS Appl. Mater. Interfaces 2018, 10, 13361−13372